



Influence of post-carburizing heat treatment on the core microstructural evolution and the resulting mechanical properties in case-hardened steel components



H. Farivar^{a,*}, M.J. Deepu^b, M. Hans^c, G. Phanikumar^b, W. Bleck^a, U. Prahl^{a,d}

^a Steel Institute (IEHK), RWTH Aachen University, Intzestr. 1, 52072 Aachen, Germany

^b Department of Metallurgical and Materials Engineering, Indian Institute of Technology Madras, 600036 Chennai, India

^c Materials Chemistry (MCh), RWTH Aachen University, Kopernikusstr. 10, 52074 Aachen, Germany

^d Institute of Metal Forming (imf), Technische Universität Bergakademie Freiberg, Bernhard-von-Cotta-Str. 4, 09599 Freiberg, Germany

ARTICLE INFO

Keywords:

Case hardening
Microstructure evolution
Toughness
Hardness
Nanoindentation
Phase field simulation

ABSTRACT

The case hardening process (carburizing followed by quenching to room temperature) is one of the heat treatments routinely conducted in various industrial sectors. Depending on the parameters applied during the post-carburizing stage, different microstructural constituents may develop in the interior (core) section of a case-hardened component which substantially influence the overall mechanical properties. In the present work, the effects of different heat treatments following the carburizing stage on the core microstructure evolution, the resulting toughness and hardness properties were investigated. The heat treatments were carried out employing Navy C-ring specimens, the core of which were used for microstructural investigations and fabrication of mini-Charpy specimens. Besides, nanoindentation tests were also carried out in the same region to examine the local hardness of different constituents. Furthermore, the microstructural evolutions were also studied utilizing multi-phase field modeling. Based on the obtained results, it can be shown that the increase in fractions of bainite and retained austenite is in direct correlation with the impact toughness improvement, however, the increase in fraction of ferrite and martensite acts inversely. Moreover, despite the differences in fractions of constituents, the level of overall hardness is similar in all the developed microstructures. Additionally, the nanoindentation results revealed that the formation of large fraction of bainitic ferrite leads to high level of scattering in nanohardness of martensite. Phase field simulations show that this is attributed to the degree of carbon partitioning into the adjacent austenitic area where depending on the local morphology and size can be quite different.

1. Introduction

In multi-phase steels it is crucial to thoroughly understand the role of microstructure in overall mechanical properties. This obviously necessitates considering the effect of heat treatment process parameters as well according to which the individual fraction and mechanical properties of each single phase is determined. The case hardening process (i.e.: carburizing followed by quenching to room temperature) is one of the common industrial thermo-chemical treatments through which the mechanical properties of the outer surface (case) is noticeably improved [1,2]. Besides a single martensitic microstructure in the case, depending on the post-carburizing parameters, a multi-phase microstructure may develop in the interior part (core) influencing the final

properties. Thus, gaining a comprehensive understanding of the heat treatment-microstructure-mechanical properties correlations is highly important enabling effective microstructural materials design.

It is well known that the core microstructure of low carbon case-hardened steel components significantly contributes to the overall performance [3–6]. For instance, such components should have sufficient toughness in their core to withstand shock loads and suppress any crack initiation which may lead to fracture. There have been numerous studies on heat treatment of low carbon low alloy steels as well as the case hardening steels where the influences of various heat treatment process parameters on mechanical properties were explored. Jiang et al. [7] investigated the effects of a novel cooling process on toughness properties of a carburizing steel. They reported that by application of a

* Correspondence to: Materials Simulation Group, Steel Institute (IEHK), Faculty of Georesources and Materials Engineering (Faculty No.: 5), RWTH Aachen University, Intzestr. 1, D-52072 Aachen, Germany.

E-mail addresses: hamidreza.farivar@iehk.rwth-aachen.de (H. Farivar), mm14d207@mail.iitm.ac.in, deepumaj@gmail.com (M.J. Deepu), hans@mch.rwth-aachen.de (M. Hans), gphan@iitm.ac.in (G. Phanikumar), bleck@iehk.rwth-aachen.de (W. Bleck), ulrich.prahl@imf.tu-freiberg.de (U. Prahl).

piecewise continuous cooling, rather than the traditional quenching and tempering process, the impact energy can considerably be enhanced. It was found out that the carbide-free lower bainite developed in the core is one of the key factors improving the toughness of the carburizing steels. Sami et al. [8] studied the microstructural changes that occur during intercritical annealing and the effects of microstructural factors on Charpy impact and tensile properties of APIX70 HSLA steel. They concluded that the characteristics of initial microstructure greatly influences the evolution of ferrite and martensite morphologies during the intercritical annealing which, in turn, influences the overall tensile and toughness properties. In another work [9] it was demonstrated that by performing an intercritical annealing step between conventional quenching and tempering treatment of a jack-up rig rack steel the ductile to brittle transition temperature significantly decreases. It was shown that the presence of upper bainite and ferrite along with high angle grain boundaries ($> 50^\circ$) and refined grain size are the main factors improving the toughness properties. Besides, based on the results obtained by Wang and co-workers [3], applying a low-temperature austempering treatment for carburizing steels is beneficial leading to improved service performance. They showed that the carburized 23Cr2Ni2Si1Mo steel when subjected to a low-temperature austempering resulted in a dual-phase microstructure of fine martensite lath and carbon-enriched retained austenite in the core which enhanced the impact toughness. Furthermore, in another research [10] the effects of initial microstructure and heat treatment on the core mechanical properties of two carburized automotive steels were investigated. The authors summarized that by conducting the normalizing treatment a slight decrease in tensile strength, a slight increase in ductility and a significant increase in impact properties of the core were obtained. Li et al. [11] discussed the effects of stress concentration in case-hardened samples on crack initiation originated from strain inconsistency between inhomogeneous core microstructure and the hardened layer.

Despite many investigations carried out in this area, a comprehensive study on the effects of different post-carburizing heat treatments, the associated hardening parameters and the resulting microstructures as well as the overall mechanical properties, however, has rarely been investigated. In the previous work of the authors [12], the effects of different hardening strategies following the carburizing stage on the quenching-induced distortion of case-hardened steel components were discussed. It was shown that by application of a modified hardening cycle the quenching-induced distortion can be reduced up to 27% while retaining the hardness properties of the case similar to that of the conventionally-hardened specimens. Further to the previous work, in the present paper, the effects of the conducted hardening cycles on the core microstructure evolution and the resulting overall toughness and hardness properties are studied. In one cycle, the quenching process is started from a fully austenitic region; in the second cycle, however, prior to the quenching, an intercritical annealing is carried out which enables ferrite to nucleate and grow out of the parent austenite in the core. Moreover, the microstructural evolutions are also simulated by means of multi-phase field modeling. The present work, therefore, aims at combined experimental and simulation investigation of heat treatment-microstructure-toughness and hardness relationships in case-hardened steel components.

2. Material and methods

2.1. Material and specimen fabrication

The chemical composition of the investigated steel is given in Table 1. The material was melted in a vacuum inductive furnace and casted in an 80 kg ingot with a dimension of $140 \times 140 \times 500$ mm 3 . The ingot was further homogenized at 1200 °C for 3 h and underwent multi-step hot forging process, producing two smaller blocks each with a final dimension of $70 \times 70 \times 1000$ mm 3 . The hot-forged blocks were thereafter exposed to normal atmosphere and air cooled to room

Table 1
Chemical composition of the investigated steel (wt%).

C	Si	Mn	P	S	Cr	Mo	Al	N	Fe
0.18	0.39	0.75	0.010	0.022	0.35	0.50	0.03	0.0069	Bal.

temperature. It was then followed by normalizing process at 900 °C to get a homogeneous microstructure. Normalized blocks were cut to smaller pieces out of which the so-called Navy C-rings were fabricated, Fig. 1. Navy C-ring specimens are frequently employed by researchers of the field to study the correlation between microstructure and heat treatment-induced distortion [13–16]. The distortion-related results of the current investigations are beyond the scope of this work and were reported elsewhere [12].

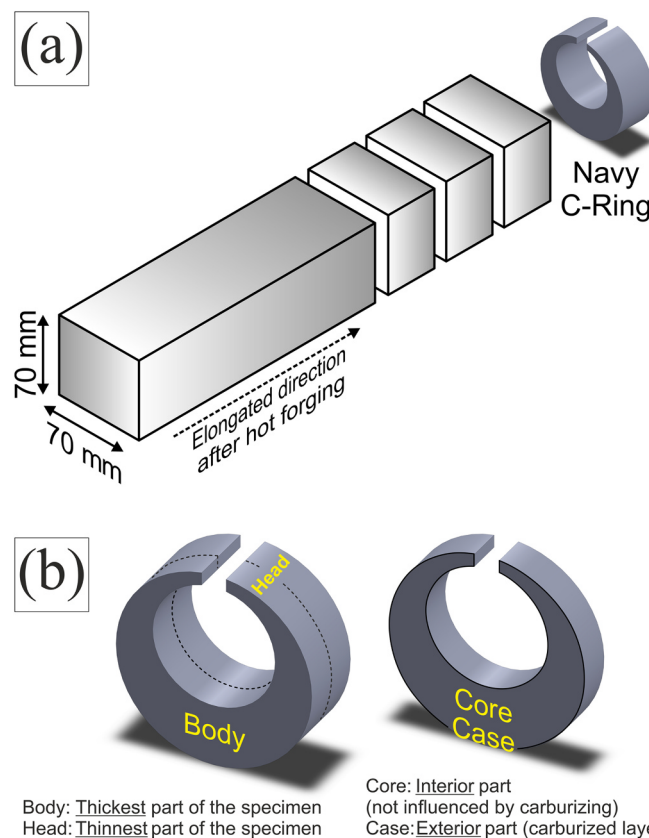


Fig. 1. (a) Schematic illustration of the produced steel block in the as-forged condition and the respective direction along which the Navy C-ring specimens were fabricated. (b) Main sections of a Navy C-ring along with the corresponding descriptions.

2.2. Heat treatment

The fabricated Navy C-rings underwent the heat treatment cycles depicted in Fig. 2, which were carried out in a dual-chamber vacuum carburizing furnace (ALD Vacuum Technologies GmbH). According to cycle A, after the carburizing stage at 950 °C the specimens were slowly cooled down to 860 °C and held isothermally for 15 min before quenching to room temperature. This batch of specimens was labeled as C860_15. However, in cycle B, the specimens were cooled down to 775 °C and held isothermally for three various times, namely, 0, 5 and 15 min which were labeled as C775_0, C775_5 and C775_15, respectively. Since the Ar₃ temperature of the base material (i.e.: core section) is 800 °C (Ar₃ measured by dilatometer), is the temperature at which ferrite starts to transform out of the parent austenite during cooling at

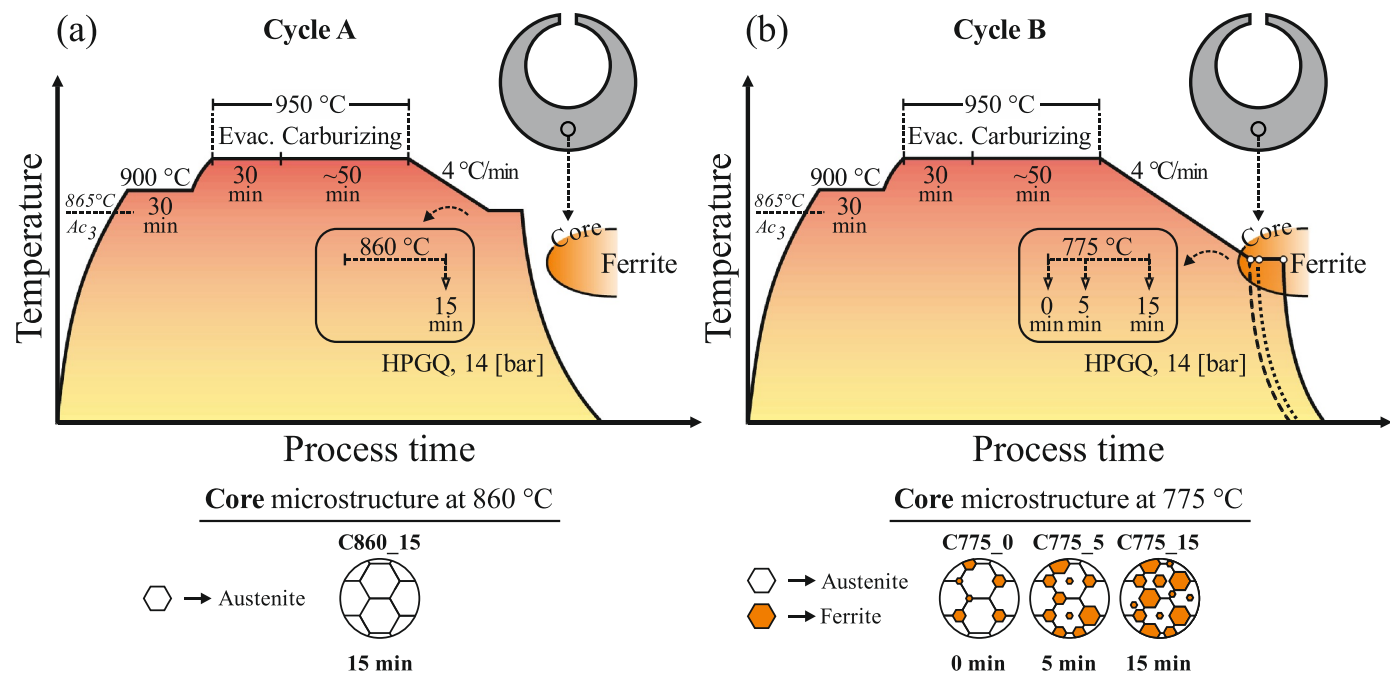


Fig. 2. (a) Cycle A where austenite in the core microstructure does not decompose at 860 °C. (b) Cycle B with the hardening temperature of 775 °C within the intercritical region where ferrite can transform out of the parent austenite in the core. (Evac.: Evacuation the atmospheric gases inside the heat treatment chamber prior to the vacuum carburizing; HPGQ: High Pressure Gas Quenching).

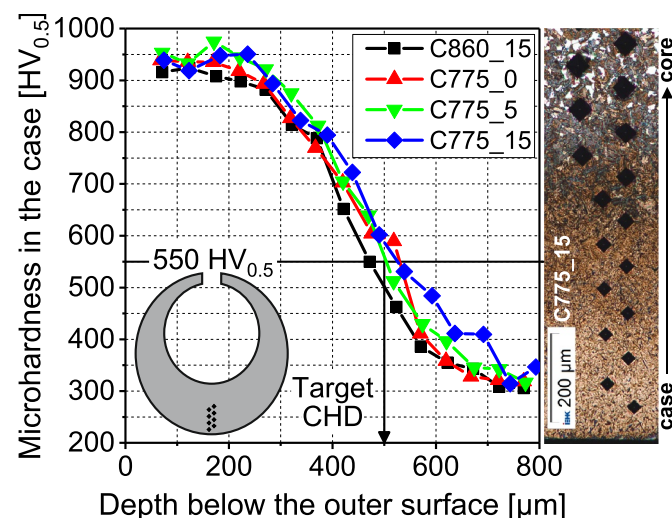


Fig. 3. Microhardness profiles in the case of the heat-treated Navy C-rings. Next to the diagram, the measurement path is exemplarily shown for ring C775_15 [12].

the rate of 4 °C/min), thus, no ferrite was expected to appear in the core microstructure of C860_15. On the contrary, by conducting the heat treatment at the hardening temperature of 775 °C, distinct fractions of ferrite could generate in the core over different holding times. It is worth mentioning that, as reported in the previous paper of the authors [12], by performing the described case hardening cycles the surface hardness properties of the Navy C-rings are maintained similar, Fig. 3.

Fig. 4 shows the time-temperature profiles captured inside of the specimens C860_15 and C775_15 while being quenched down to room temperature. The data were collected by means of a high temperature measurement system (PhoenixTM®) including a thermal barrier box (TS02-235 QD), N-type thermocouple and a data logger (PTM1010). The profile obtained for C775_15 is representative for specimens C775_0 and C775_5 too, since they were quenched from the identical temperature (775 °C).

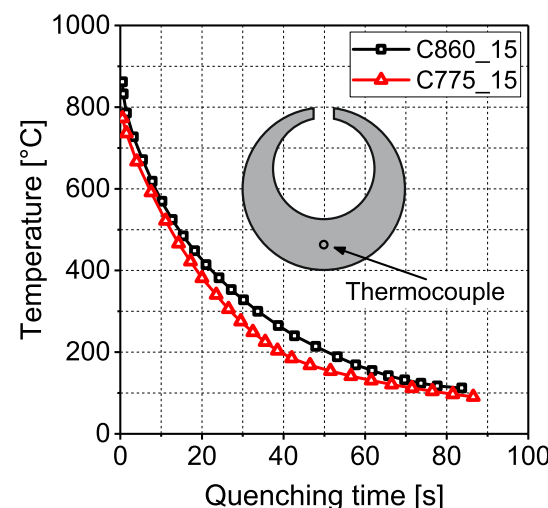


Fig. 4. Time-temperature profiles measured in the interior region (core) of the selected Navy C-rings during the quenching stage.

2.3. Microstructural analysis

The heat-treated rings were cross-sectioned and metallographically prepared (grinding, polishing and etching with 3% Nital) for microstructural analysis in the core region using light optical microscope (LOM) and scanning electron microscopy (SEM). Besides, the microstructure and crystallographic texture characteristics were studied more in detail employing electron backscatter diffraction (EBSD) technique. Therefore, the samples were beforehand polished in multiple steps to prepare a flat and scratch-free surface. The EBSD measurements were carried out by means of a Schottky field-emission gun SEM, JEOL JSM-7000F (JEOL Ltd) operated at 20 kV and a step size of 100 nm.

2.4. Mechanical tests

Using spark erosion method mini-Charpy V-notch specimens (known as KLST specimens, Kleinstproben, DIN 50115) were manufactured out of the core of the heat-treated C-rings' thickest section (Body) to evaluate the impact toughness of the developed microstructures, Fig. 5. To generate sufficient statistical data, impact tests were performed for six KLST specimens (fabricated out of two rings, three KLST specimens each) per each heat treatment cycle at room temperature employing a Zwick's HIT50 instrumented impact machine with a 50 J pendulum.

Moreover, the overall hardness properties of the developed microstructures were inspected by means of a typical hardness equipment (HV₁₀). Additionally, local hardness of the microstructural constituents was measured by nanoindentation using a Hysitron TI-900 TriboIndenter with a performech™ I Advanced Control Module. 250 μN maximum load was applied for each indentation using a cube-corner diamond tip with 40 nm radius. The tip area calibration was conducted by indentation on fused silica before and after the measurements [17].

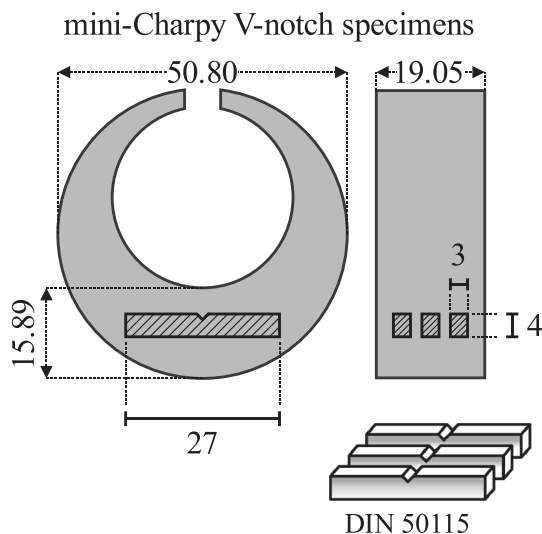


Fig. 5. Schematic illustration of the mini-Charpy V-notch specimens (DIN 50115) fabricated out of the core of the case-hardened C-rings' thickest section. (All dimensions in mm).

2.5. Multi-phase field modeling of microstructure evolution

A multi-phase field model implemented in the software MICRESS® [18] was utilized to simulate the microstructure evolution during the isothermal stage of the heat treatment cycles and also during the subsequent quenching to room temperature. For the austenite to ferrite transformation the required thermodynamic and kinetic data were provided by coupling with the databases of Thermo-Calc®, namely, TCFE7 and MOBFE3, respectively. For the simulation of bainite transformation the required thermodynamic data was likewise provided by TCFE7, whereas, the necessary kinetic data were taken from literature [19]. 2D simulations were performed in an $80 \times 80 \mu\text{m}^2$ domain size, a grid size of $0.1 \mu\text{m}$ and with periodic boundary conditions. Voronoi tessellation was used to create an initial microstructure with a single austenitic phase. This resembles the starting microstructure at the beginning of the cooling stage from 950 °C down to 860 °C (cycle A) and 775 °C (cycle B), as shown in Fig. 2. The distribution of Voronoi seeds and the corresponding radius were selected in such a way as to reproduce the average prior grain size of austenite ($20 \mu\text{m}$) obtained from

Table 2

Nucleation parameters used for the simulation of bainite transformation.

Microstructure	C860_15	C775_0	C775_5	C775_15
Nucleation undercooling (K)	120	110	125	172
Shield distance (μm)	2.6	2.4	2.0	1.5

the experimental micrographs. Random orientation was assigned to the grains in the initial microstructure. NPLE (Negligible Partitioning Local Equilibrium) assumption was used to consider the mixed mode character of the transformation where interfacial mobility was used as an adjustable parameter.

At the initial stage, the simulation of austenite decomposition into ferrite during the temperature reduction from 950 °C down to 860 °C and 775 °C was performed with the cooling rate adopted from the experiments (4 °C/min) and followed by holding at the hardening temperatures for the respective durations. A shield distance of 20 μm and a shield time of 20 s was used to simulate the nucleation of ferrite. The interfacial energy and the interfacial mobility used for the austenite to ferrite transformation were $\sigma_0^{\gamma\alpha} = 4.0 \times 10^{-5} \text{ J/cm}^2$ and $\mu_{\phi}^{\gamma\alpha} = 2.0 \times 10^{-5} \text{ cm}^4/\text{Js}$, respectively. Moreover, the simulation of microstructure evolution was further continued during the quenching stage based on the experimentally-obtained thermal profiles (Fig. 4). Using anisotropy functions, the bainite morphology and the formation of retained austenite was described. Due to high computational costs no carbide (e.g.: cementite) formation was considered in the present simulations. Bainite was considered to nucleate and grow in the form of sheaf at all the grain boundaries and at the bulk. Critical undercooling for nucleation was used as a tuning parameter to match the bainite start temperature with the experimentally-measured data. Furthermore, the subunits of the bainite sheaves were assumed to have identical crystallographic orientation and habit plane [20]. The shield parameter was used as another tuning parameter to reproduce the bainite sheaf mimicking the experimentally-observed morphology. Table 2 shows the nucleation parameters used for the bainite transformation simulation.

The temperature dependence of the interfacial mobility (μ_{ϕ}^{By}) for the simulation of austenite to bainite transformation was described by an Arrhenius relationship as:

$$\mu_0^{By} = \mu_{\phi}^{By} \exp\left(\frac{-Q}{RT}\right) \quad (1)$$

where $\mu_{\phi}^{By} = 0.9 \text{ cm}^4/\text{Js}$, is the pre-exponential factor for mobility, and $Q = 92.2 \text{ kJ/mol}$ [19], is the activation energy. μ_{ϕ}^{By} is an adjustable parameter and the value was chosen based on the best fit between simulated and experimental phase fractions of bainite. R is the gas constant and T is the temperature in Kelvin. Anisotropic interfacial energy ($\sigma^{By}(\vec{n})$) and anisotropic interfacial mobility ($\mu^{By}(\vec{n})$) were considered to reproduce the bainite sheaf morphology. The interfacial energy and interfacial mobility were considered as a function of normal to the interface of the grain (\vec{n}) in local coordinate system [21] as:

$$\sigma^{By}(\vec{n}) = \sigma_0^{By} a^{\sigma}(\vec{n}) \quad (2)$$

$$\mu^{By}(\vec{n}) = \mu_0^{By} a^{\mu}(\vec{n}) \quad (3)$$

where $\sigma_0^{By} = 5.0 \times 10^{-5} \text{ J/cm}^2$ [20], is the constant value of the interfacial energy. $a^{\sigma}(\vec{n})$ and $a^{\mu}(\vec{n})$ are tetragonal anisotropy functions and are given by:

$$a^{\sigma}(\vec{n}) = [1 \pm 4\delta_1^{\sigma}(n_x^4 + n_y^4 + n_z^4 - 0.75)](1 - n_z^2 - \delta_2^{\sigma} n_z^2) \quad (4)$$

and similarly, for $a^{\mu}(\vec{n})$. This is an inbuilt anisotropy function in the software MICRESS®. Anisotropy parameters used for interfacial energy were $\delta_1^{\sigma} = 0.1$ and $\delta_2^{\sigma} = 0.5$, whereas, for mobility, $\delta_1^{\mu} = 0.2$ and

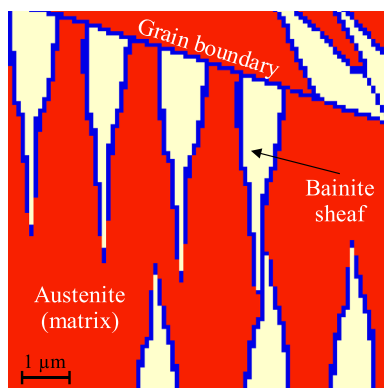


Fig. 6. The simulated morphology of bainite sheaves.

$\delta_2^{\mu} = 0.05$ were used. n_x , n_y and n_z represent the x, y and z coordinates. Anisotropy parameters were chosen based on the best fit between the simulated and experimental bainite sheaf morphology. Fig. 6 shows the typical morphology of bainite sheaves obtained with the anisotropy functions used.

Besides, in order to determine the fraction of austenite which is retained after quenching to room temperature (20°C), the well accepted equation derived by Koistinen-Marburger was used [22]. The respective martensite start temperature (M_s) was also calculated using an empirical relation as described in Eq. (5) [23]. For the austenitic areas with a M_s above room temperature, the austenite either fully transforms to martensite or a part of it may retain. However, for those areas with a M_s below room temperature, the austenite is fully retained. The minimum amount of carbon required to fully stabilize the austenite at room temperature (critical carbon concentration) was calculated to be 1.14 wt%.

$$M_s(\text{°C}) = 539 - 423C - 30.4Mn - 17.7Ni - 12.1Cr - 11Si - 7Mo \quad (5)$$

where all the alloy contents (C, Mn, Ni, Cr, Si and Mo) are in weight percent (wt%). After calculation of the fraction of retained austenite, it was assumed that the remaining austenite transformed to martensite.

3. Results

3.1. Microstructural characterizations

Fig. 7 shows the light optical micrographs (LOM) of the investigated microstructures. In C860_15 no ferrite (F) was identified and the microstructure is a mixture of bainite (B) and martensite (M). However, for the specimens which were intercritically annealed at 775°C , ferrite transformed out of the parent austenite. Furthermore, it is evidently seen that by increasing the isothermal holding time the fractions of ferrite (f^F) and martensite (f^M) monotonically increase, whereas, the fraction of bainite (f^B) decreases. The quantitative fractions of the developed phases are summarized in Table 3. The volume fractions of the microstructural constituents were quantified by applying the point-counting method on at least five representative micrographs [24].

Fig. 8 displays the crystallographic textures of the developed microstructures analyzed by EBSD. It is obviously seen that by reducing the temperature from 860°C down to 775°C ferrite phase which is corresponding to the area with a higher image quality (IQ) appeared in the microstructure and advanced over time. This is more evident in the calculated kernel average misorientation (KAM) maps where the fraction of regions with a lower KAM values (representing ferrite) increases over time at 775°C . It should also be noted that by performing a longer holding time at 775°C , besides reduction in bainite fraction, the fraction of retained austenite (f^{RA}) diminishes too. The indexed fractions of retained austenite are 3.6%, 2.8%, 1.8% and 0.3% in C860_15, C775_0, C775_5 and C775_15, respectively. Hence, it is inferred that there is a direct correlation between the fraction of bainite and the fraction of retained austenite. Both typical morphologies of retained austenite, known as film-like and blocky shape are present in the developed microstructures.

Table 3

The quantitative volume fractions of the microstructural phases (point-counting method).

Specimen	Ferrite (F)	Bainite (B)	Martensite (M)
C860_15	—	86 ± 5%	14 ± 5%
C775_0	6 ± 2%	77 ± 4%	17 ± 3%
C775_5	20 ± 5%	51 ± 3%	29 ± 4%
C775_15	30 ± 2%	23 ± 3%	47 ± 2%

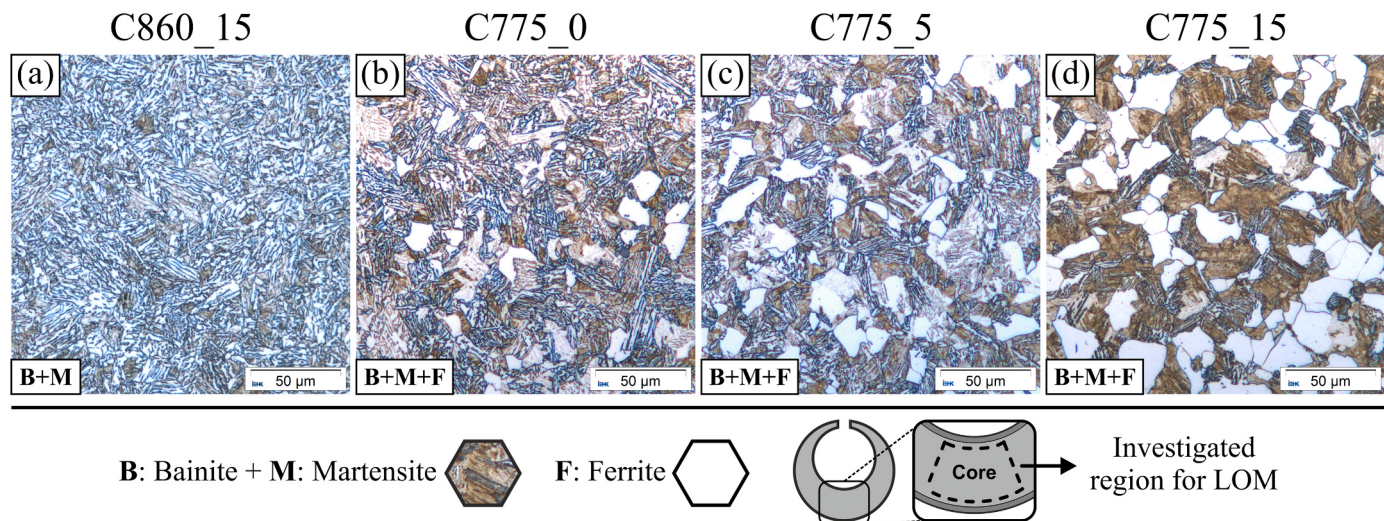


Fig. 7. Light optical micrographs (LOM) of the investigated microstructures in (a) C860_15, (b) C775_0, (c) C775_5 and (d) C775_15.

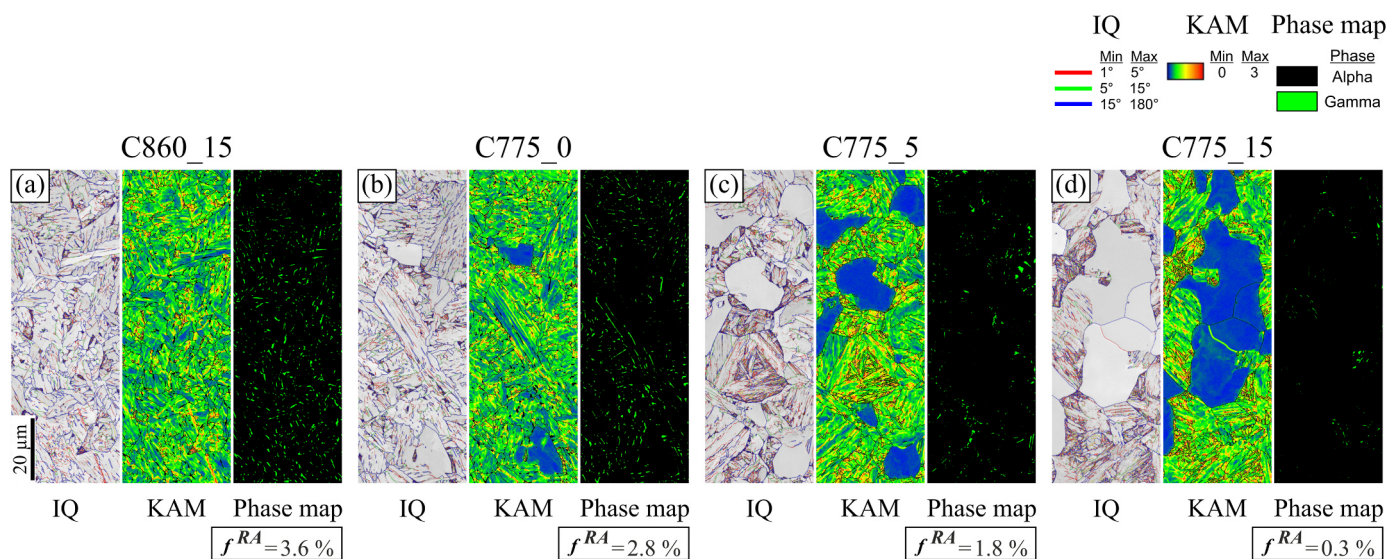


Fig. 8. EBSD results of the investigated microstructures in (a) C860_15, (b) C775_0, (c) C775_5 and (d) C775_15. Image Quality (IQ) maps, calculated Kernel Average Misorientations (KAM) maps and Phase maps are respectively shown for each microstructure. The KAM values are calculated with a step size of 100 nm and over a radius of 300 nm with a maximum misorientation of 5°. Note that the presented volume fraction of retained austenite (f^{RA}) in each case was determined from a larger measurement area ($100 \times 100 \mu\text{m}^2$) than what is displayed in this figure.

3.2. Mechanical properties

3.2.1. Charpy impact properties

The load-displacement curves obtained during the dynamic impact mini-Charpy tests along with their corresponding key characteristics are presented in Fig. 9. Each curve can be divided into two parts; (i) area beneath the curves from the beginning up to the point of maximum load (F_{max}) which reflects the energy consumed by a microstructure during crack initiation, E_i ; (ii) area beneath the curves from the maximum load until the end point of the curve which represents the energy consumed by a microstructure to resist crack propagation, E_p . The total

energy (E_t) absorbed by a microstructure is therefore the summation of the terms E_i and E_p . All main impact properties are summarized in Table 4 for a better comparison.

As shown in Fig. 9 and Table 4, mini-Charpy specimens C860_15 demonstrate the largest F_{max} , E_i and E_p values as compared to the other specimens. Among the ferrite-containing specimens, which were intercritically annealed at 775 °C for different durations, the one with the shortest holding time (C775_0) shows the best toughness properties, but, less than C860_15. Furthermore, with extending the holding time at 775 °C the toughness properties get proportionally degraded. Besides, by reducing the temperature from 860 °C to 775 °C and applying longer holding time, the relative contribution of energy consumption by crack initiation (E_i/E_t) monotonically increases, whereas, the relative contribution of energy absorption by crack propagation (E_p/E_t) decreases.

The SEM fractographs of the ruptured mini-Charpy specimens are presented in Fig. 10. The macro-fractographs are displayed in Fig. 10a-d. The fracture surfaces just beneath the notch root (labeled as Area 1) are shown in Fig. 10e-h. As it is observed, except specimen C775_15, which clearly revealed a mixed ductile-brittle mechanism in Area 1, Fig. 10h, in rest of the broken specimens the fracture mode in the mentioned area are entirely ductile with the typical dimples, Fig. 10e-g. Besides, the area within the ruptured surface of each specimen where brittle fracture was firstly observed (labeled as Area 2), Fig. 10i-l, was detected and its corresponding distance from the notch root (d) was accordingly measured. In specimen C860_15, d is approximately $620 \pm 85 \mu\text{m}$ and progressively decreases in the other specimens which were intercritically annealed at 775 °C and read as follows: $550 \pm 75 \mu\text{m}$ and $460 \pm 90 \mu\text{m}$ for C775_0 and C775_5, respectively. As pointed out above, in specimen C775_15 the cleavage areas and dimples exist together directly below the notch root in a mixed ductile-brittle mode, hence, d for C775_15 equals 0.

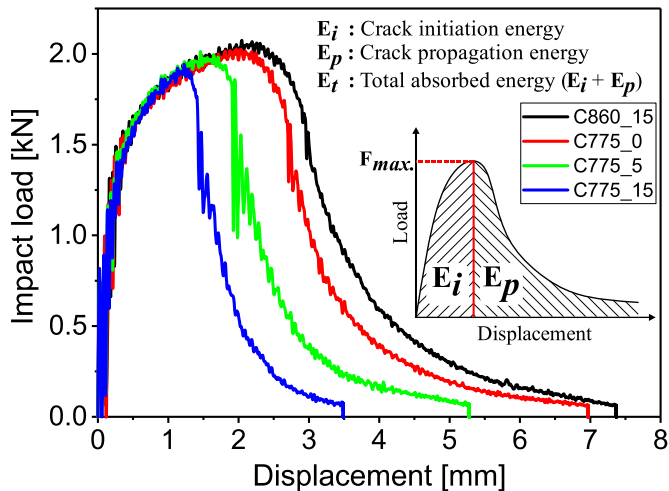


Fig. 9. The recorded load-displacement curves of the investigated mini-Charpy V-notch specimens during impact tests.

Table 4

Impact toughness properties of the investigated specimens.

Specimen	F_{max} (kN)	E_i (J)	E_p (J)	E_t (J)	E_i/E_t (%)	E_p/E_t (%)
C860_15	2.07 ± 0.06	3.45 ± 0.2	3.57 ± 0.1	7.02 ± 0.2	49	51
C775_0	2.02 ± 0.02	3.34 ± 0.3	2.84 ± 0.4	6.18 ± 0.4	54	46
C775_5	1.95 ± 0.03	2.48 ± 0.3	2.02 ± 0.3	4.50 ± 0.3	55	45
C775_15	1.91 ± 0.04	1.82 ± 0.4	1.25 ± 0.4	3.07 ± 0.4	59	41

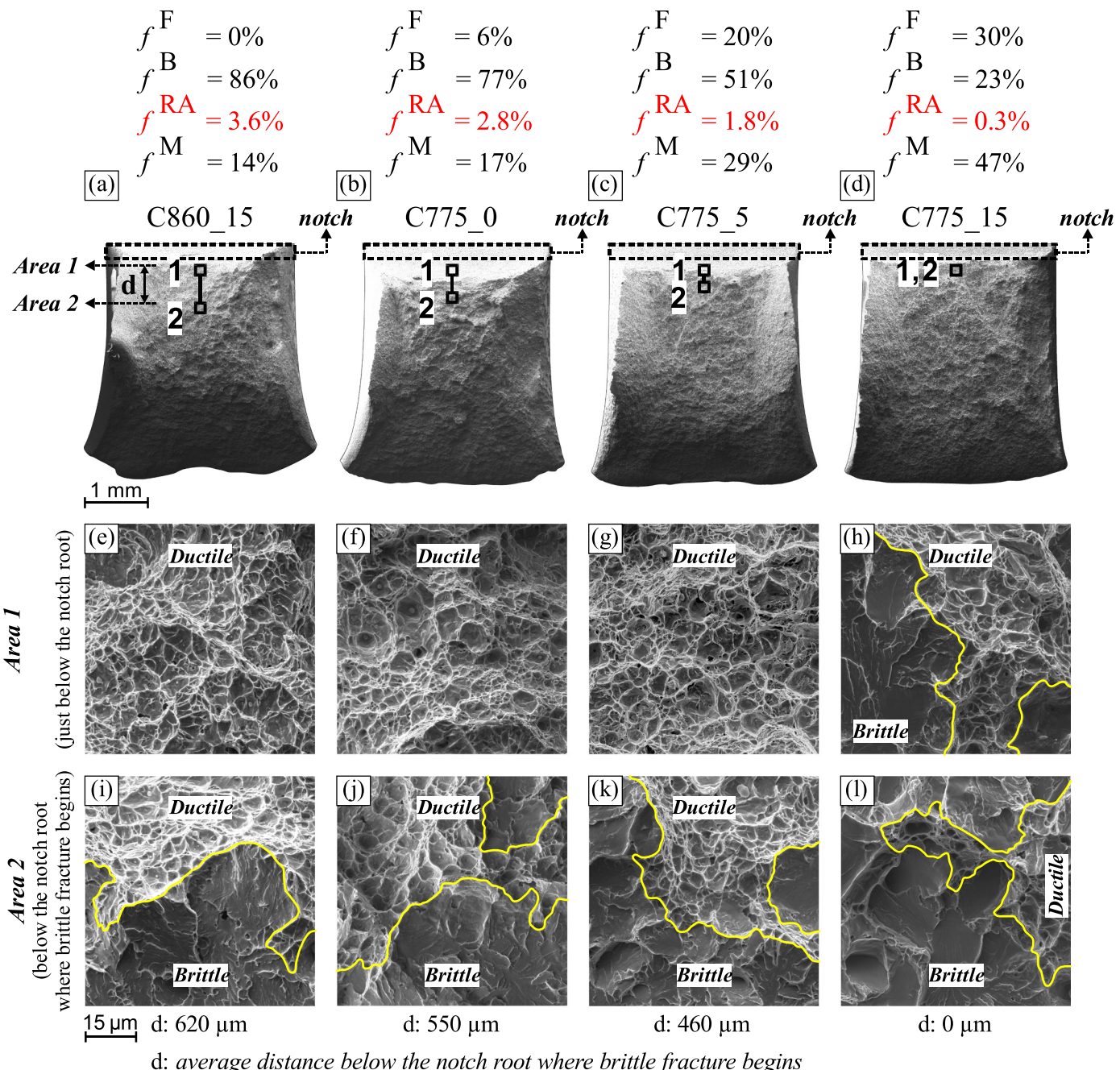


Fig. 10. SEM fractographs of the broken mini-Charpy V-notch specimens. The macro-fractographs of the specimens are in (a-d) above which the corresponding fractions of constituents in each case are also indicated. It should be noted that the presented fractions of retained austenite (f^{RA}) are a part of the bainite which were distinguished and quantified through EBSD analyses. The area just beneath the notch root (Area 1), the area within the ruptured surface where brittle fracture was firstly detected (Area 2) and the length difference between these two areas (d) are indicated. The magnified images of the fracture morphologies in Area 1 and Area 2 are in (e-h) and (i-l), respectively.

3.2.2. Hardness measurements

The overall Vickers hardness (HV_{10}) of the developed microstructures are presented in Table 5. It is readily deduced that despite substantial differences in volume fractions of microstructural phases (Table 3), the overall hardness values remain almost constant.

Fig. 11a shows the results of nanoindentation tests on the martensite (M), bainitic ferrite (BF) and ferrite (F) of two selected samples, namely, C860_15 and C775_15, the microstructural constituents of which are present at their extreme fractions (Table 3). In Fig. 11(b–c) the SEM images of the investigated microstructures along with the nanoindentation impressions in various phases are displayed. It is seen that the average local hardness of martensite (M) in C860_15

(6.8 ± 1.5 GPa) is higher than that in C775_15 (6.0 ± 0.6 GPa). It is, however, to be noted that a larger degree of scattering in martensite hardness is present in the former as compared to that in the latter (note the error bars indicating the values of standard deviations). According to the evaluated data, nanohardness of bainitic ferrite (BF) in C860_15

Table 5
Overall hardness values of the investigated microstructures.

Specimen	C860_15	C775_0	C775_5	C775_15
Hardness [HV_{10}]	274 ± 6	267 ± 5	265 ± 6	269 ± 5

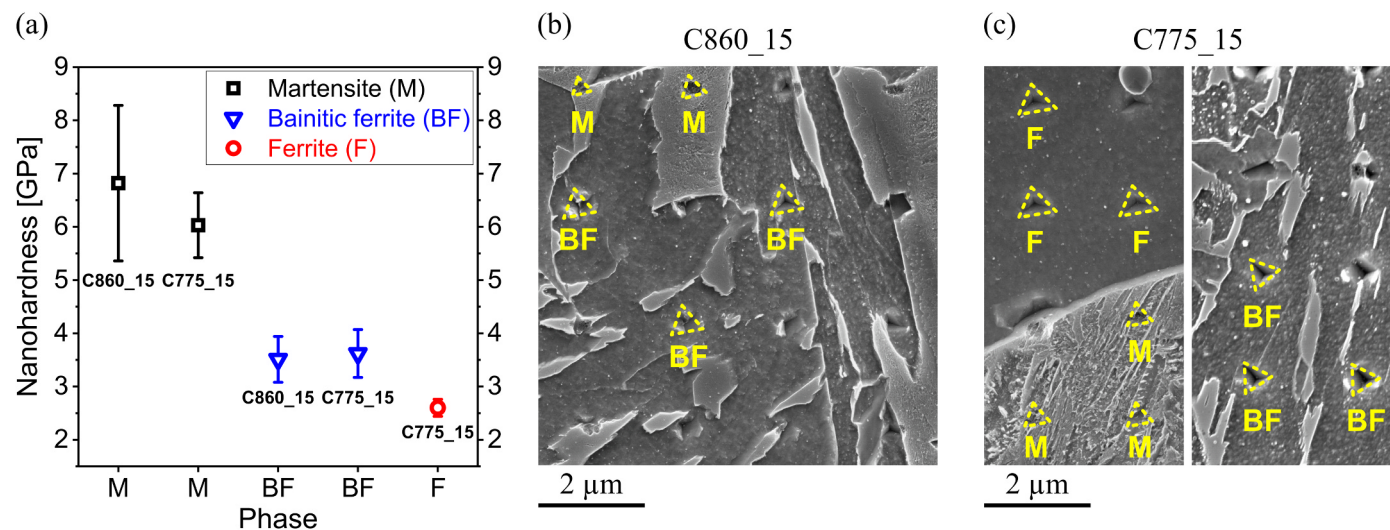


Fig. 11. The average nanohardness values of the constituent phases in C860_15 and C775_15 along with the corresponding standard deviations (error bars) are in (a). The SEM images showing the nanoindentation impressions in individual phases of C860_15 and C775_15 revealed by Nital etching are in (b) and (c), respectively. Note that only those successful indentations (indicated by triangles) were considered for the respective analyses.

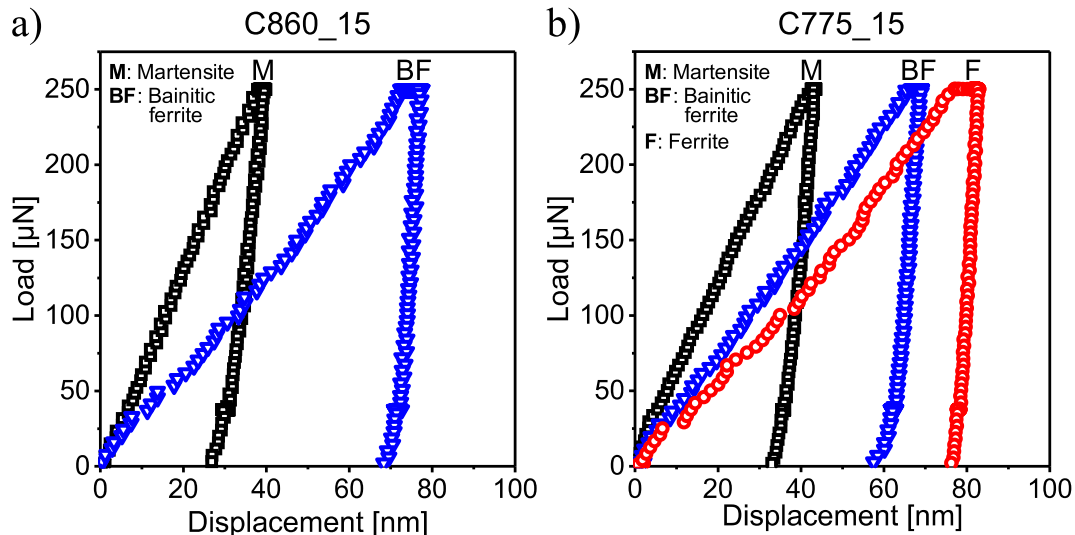


Fig. 12. Representative examples of the load-displacement curves obtained during the nanoindentation tests in Martensite (M), Bainitic ferrite (BF) and Ferrite (F) of C860_15 and C775_15 are in (a) and (b), respectively.

$(3.5 \pm 0.4 \text{ GPa})$ is similar to that in C775_15 ($3.6 \pm 0.5 \text{ GPa}$). Furthermore, the nanohardness of ferrite (F), which was intercritically transformed in C775_15, was measured to be $2.6 \pm 0.2 \text{ GPa}$.

The differences in local hardness of the microstructural phases are more obvious in Fig. 12 where representative examples of the load-displacement curves obtained for the investigated phases are plotted. As shown in Fig. 12(a–b), the final indentation depth in martensite (M) of C860_15 and C775_15 were recorded to be 27 nm and 33 nm, respectively, which are consistent with the above-mentioned nanohardness values. This quantity in bainitic ferrite (BF) of C860_15 was measured to be 68 nm, however, this is 58 nm for its counterpart in C775_15. Furthermore, the final indentation depth in ferrite (F) was measured to be 76 nm in C775_15 which is the largest amongst the investigated constituents implying its lowest resistance against indentation penetration and thus, the lowest nanohardness, as described above.

3.3. Multi-phase field simulations

The results of multi-phase field simulations are shown in Fig. 13. The simulated microstructural constituents including ferrite, bainitic ferrite and the mixture of martensite and retained austenite are displayed in Fig. 13(a–d). The corresponding carbon concentration and retained austenite maps are also shown in Fig. 13(e–h) and Fig. 13(i–l), respectively. As shown in the phase maps, Fig. 13(a–d), no ferrite appears in C860_15, whereas, the fraction of ferrite progressively increases by extending the holding time at 775 °C. The same also holds true for martensite. The evolution of bainitic ferrite, however, follows an inverse trend. Furthermore, as a result of ferrite and bainite formation, the respective carbon atoms are rejected and then accommodated in the adjacent austenitic regions where depending on the local morphology the level of carbon enrichment can be quite different, Fig. 13(e–h). During the final stages of the quenching process, depending on the local carbon content, a part of such carbon-enriched

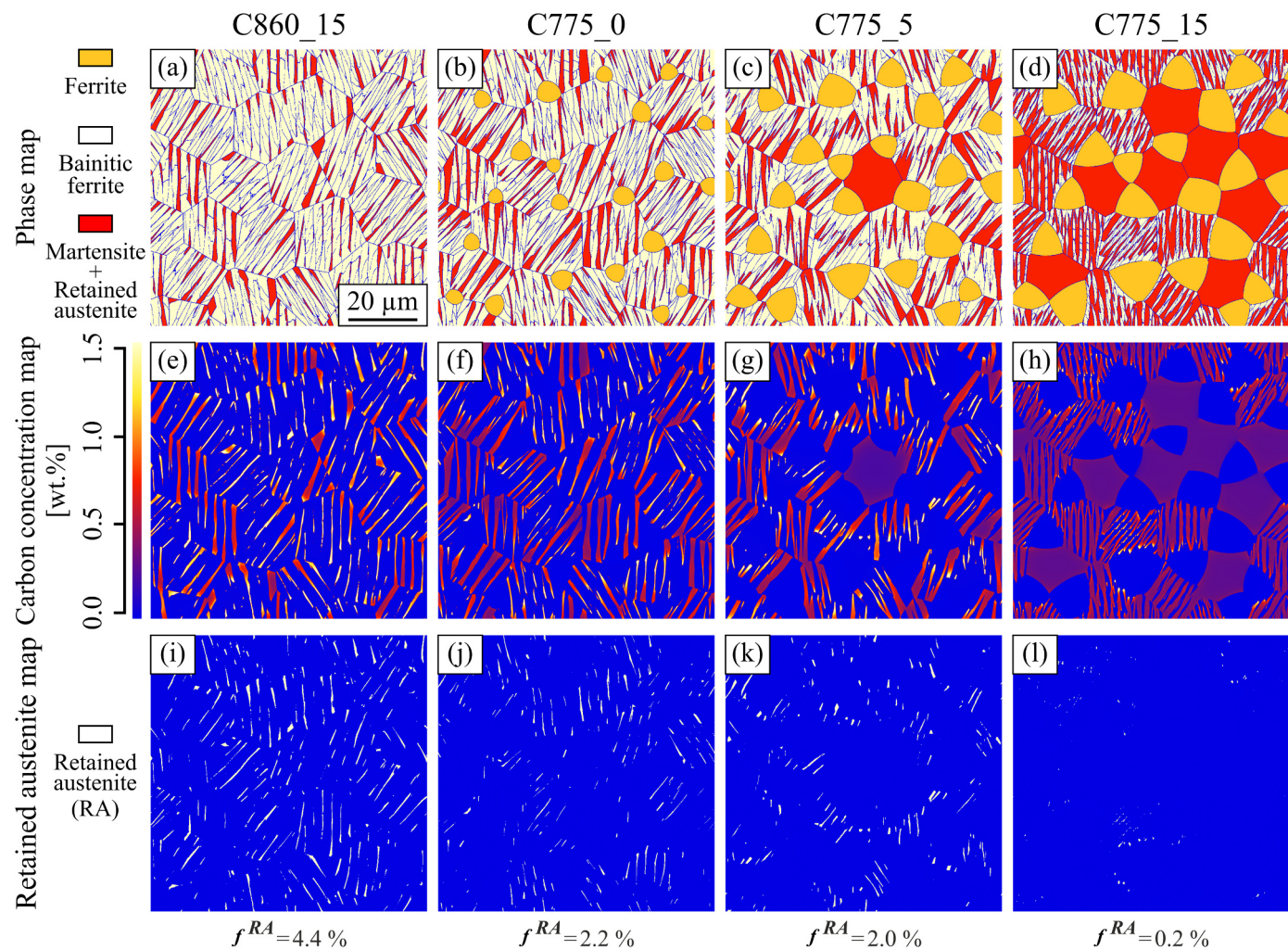


Fig. 13. Simulated microstructural constituents including ferrite, bainitic ferrite and the mixture of martensite and retained austenite are in (a–d). The corresponding carbon distributions are in (e–h). The predicted retained austenite (RA) maps are in (i–l).

regions may transform to martensite and the rest is retained (retained austenite, RA). According to the retained austenite maps, Fig. 13(i–l), the fraction of this phase is at the highest in C860_15 (4.4%) and gradually diminishes in the ferrite-containing microstructures subjected to the longer holding times; 2.2%, 2.0% and 0.2% in C775_0, C775_5 and C775_15, respectively. Moreover, it is readily observed that the fraction of retained austenite (f^{RA}) is directly proportional to the fraction of bainitic ferrite, but, in an inverse proportion to the fraction of ferrite and martensite. The quantitative fractions of all the simulated phases along with the corresponding experimentally-obtained values are listed in Table 6 showing a very good agreement between the simulated and experimental data.

4. Discussion

4.1. Heat treatment-microstructure correlation

During the isothermal stage at 860 °C (cycle A), austenite is stable solely and does not undergo any phase transformation. Further, during the quenching stage, austenite, however, transforms to different phases including bainite and martensite and a part of it is left as retained austenite. On the contrary, however, at 775 °C (cycle B) ferrite is thermodynamically favored and therefore, can nucleate and progressively grow by extending the holding time. Due to the low carbon solubility of ferrite, while it develops, the excess carbon atoms are

Table 6

The volume fractions of the microstructural constituents predicted by the phase field modeling (Sim.) in comparison with the corresponding experimentally-obtained values (Exp.).

Microstructure	Ferrite (F)		Bainite (B)		Martensite (M)		Retained austenite (RA)	
	Sim.	Exp. (LOM)	Sim. ^a	Exp. (LOM)	Sim.	Exp. (LOM)	Sim.	Exp. ^b (EBSD)
C860_15	–	–	86%	86 ± 5%	9.6%	14 ± 5%	4.4%	3.6%
C775_0	8%	6 ± 2%	73%	77 ± 4%	16.8%	17 ± 3%	2.2%	2.8%
C775_5	21%	20 ± 5%	56%	51 ± 3%	21.0%	29 ± 4%	2.0%	1.8%
C775_15	29%	30 ± 2%	24%	23 ± 3%	46.8%	47 ± 2%	0.2%	0.3%

^a The simulated fractions of B presented here are basically the values of bainitic ferrite.

^b The presented fractions of RA are a part of the bainite which were distinguished and quantified through EBSD analyses.

rejected and accommodated in the adjacent austenitic regions, with higher carbon solubility. The longer the intercritical holding time at 775 °C, the larger fraction of ferrite is created and hence, a higher level of chemical stability is attained in austenite prior to the quenching. This retards and restricts the subsequent diffusional phase transformation of bainite and promotes the formation of martensite instead. Thus, depending on duration of the holding time and the level of carbon enrichment in austenite, different fractions of microstructural constituents are developed under the same quenching conditions. This explains the differences and the trends observed in fractions of microstructural phases (Table 3).

Besides, as it was shown in Section 3.1, there is a direct relation between the fraction of bainite and retained austenite. As it is well documented in the literature, bainite is a mixture of plate-like ferrite (can also have carbide in it, known as lower bainite) separated by retained austenite, martensite or cementite, the development of which can be described by a combined displacive and diffusional mechanism [25,26]. Therefore, due to the formation of bainitic ferrite the excess carbon atoms are partitioned into the neighboring austenite raising its chemical stability [27,28]. Depending on the local chemical composition, morphology and dislocation density of this carbon-enriched austenite, a part of it may decompose to carbides and the other part may either transform to martensite or retain. The retention of austenite, thus, is more plausible in the microstructures where higher fractions of bainite are generated. This elucidates the experimentally-observed results in the present work (Fig. 8). It is worth mentioning that the overall intensity of carbon enrichment in the austenite of C860_15 with 82% bainitic ferrite is much larger than that of C775_15 with 30% intercritically-transformed ferrite and 23% bainitic ferrite (i.e.: 53% in total). This also agrees well with the outcomes of the phase field modeling which showed that in C860_15, where larger fraction of bainitic ferrite is developed, there exist many regions which are severely enriched with carbon atoms leading to higher fraction of retained austenite as compared to the ferrite-containing microstructures (Fig. 13 and Table 6). Since the fraction of bainitic ferrite monotonically decreases in C775_0, C775_5 and C775_15, thus, the level of carbon enrichment induced by this phase decreases as well, hence, the reduction in fraction of retained austenite.

4.2. Microstructure-mechanical properties correlation

It is well known that by making the microstructure more chaotic the propagating cracks can frequently be deflected, hence, improving the crack propagation resistance [9,29,30]. In this regard, bainite as a microstructural aggregate comprised of bainitic ferrite plates with different orientations and intervening film-like retained austenite plays a significant role. The effectiveness of bainitic sheaves are basically due to their ability to constantly deviate crack propagation path which is, in turn, caused by various crystallographic orientations and grain boundaries of sub-structures [7]. Besides, upon the arrival of crack tip at the film-like retained austenite, it may transform to martensite (transformation-induced plasticity: TRIP effect) dissipating the energy which would be used for crack advancement [31–33]. Furthermore, the newly generated martensite also deflects the propagating crack. Hence, bainite significantly contributes to the overall toughness properties. This agrees well with the results of mini-Charpy impact tests (Fig. 9 and Table 4) where larger amount of energy was dissipated in C860_15 during the crack initiation and propagation stages as compared to the other microstructures. This is attributed to the higher fraction of bainite and retained austenite present in C860_15, as confirmed by EBSD results (Fig. 8), in comparison to the other specimens. The amount of bainite and retained austenite continuously decrease in specimens C775_0, C775_5 and reach the minimum in C775_15, hence, their toughness properties monotonically decrease. The effectiveness of bainite and retained austenite in toughness properties was also evident by analyzing the fracture surfaces of the mini-Charpy specimens (Fig. 10).

It was clearly shown that in specimen C860_15, with the highest fraction of bainite and retained austenite, the onset of brittle fracture was more retarded in comparison to the other specimens. In fact, the widest area where a ductile mechanism is dominant (d) belongs to specimen C860_15 which thereafter gets narrower consecutively in specimens C775_0, C775_5 and C775_15. This implies a wider crack initiation site, in other words, a higher resistance against crack initiation in C860_15 as compared to the ferrite-containing microstructures.

Moreover, in specimens C775_0, C775_5 and C775_15 the fractions of ferrite and martensite both progressively increase. This, in turn, increases the fraction of ferrite-martensite grain boundaries with severe hardness difference which facilitates the nucleation and progress of secondary cracks. Besides, it is well known that increasing the fraction of martensite as a brittle phase degrades toughness of a material [34]. Hence, impact toughness properties in the ferrite-containing specimens proportionally decline by increasing the fractions of ferrite and martensite.

As it was presented in Table 5, irrespective of the differences in fractions of microstructural constituents, the level of overall hardness (HV_{10}) is similar in all the specimens. In C860_15, the microstructure was mostly comprised of bainite and the overall hardness, therefore, largely dominated by this phase. In specimens C775_0, C775_5 and C775_15 the fraction of ferrite, as a soft phase, monotonically increases expecting to decrease the overall hardness; whereas, the fraction of martensite, as a hard phase, simultaneously increases too. This compensates the overall hardness drop which could originate from increasing the fraction of ferrite, and hence, keeps the overall hardness in all of the investigated specimens at a similar level.

Due to the formation of large amount of bainite (B) in C860_15 (approx. 86%), many carbon atoms are accordingly partitioned into the adjacent austenitic regions enhancing the local hardness of the resulted martensite [35]. Depending on the local morphology and size of these austenitic zones, the level of carbon uptake can be quite different. This may lead to severe carbon enrichment in small austenitic regions and heterogeneous carbon distribution in some coarser zones in which carbon atoms have to diffuse farther to get equally dispersed [36–38]. But, due to the low diffusivity of interstitial carbon atoms in FCC structure of austenite, this may hardly be realized during the course of the quenching; hence, heterogeneous local hardness in martensite [37,39,40]. This justifies the large degree of scattering in nanohardness of martensite ($\pm 1.5 \text{ GPa}$) observed in C860_15. These arguments were also supported by the phase field simulations which showed that the level of carbon enrichment in smaller austenitic regions of C860_15 are substantially high (approx. 0.8 wt%) and it decreases if the austenite gets larger, Fig. 14 (line a). It is worth pointing out that in some austenitic areas, the carbon concentration is beyond the critical value (1.14 wt%) and thus, austenite is fully retained. Furthermore, the bigger austenitic regions are more susceptible to the formation of sharp carbon gradients, where the marginal zones are decorated with higher amount of carbon atoms (up to 0.6 wt%) and then gradually declines towards the interior parts with an approximate concentration of 0.4 wt %, Fig. 14 (line b). Besides, in C775_15, the average nanohardness of martensite and the associated level of scattering diminish which is due to the lower total fraction of bainite (B) and ferrite (F) which caused less overall carbon rejection, hence, lower level of carbon enrichment and also lower carbon inhomogeneity. As shown in Fig. 14 (lines c and d), the overall level of carbon enrichment in C775_15 is lower than that in C860_15, hence, lower average nanohardness of martensite in C775_15 as compared to C860_15 ($6.0 \pm 0.6 \text{ GPa} < 6.8 \pm 1.5 \text{ GPa}$). Additionally, as predicted by the simulations, it is revealed that regardless of the austenite size, the carbon atoms are much more homogeneously distributed in the austenitic areas of C775_15. This, therefore, explains the lower level of scattering in martensite of C775_15 as compared to that of C860_15 ($\pm 0.6 \text{ GPa} < \pm 1.5 \text{ GPa}$).

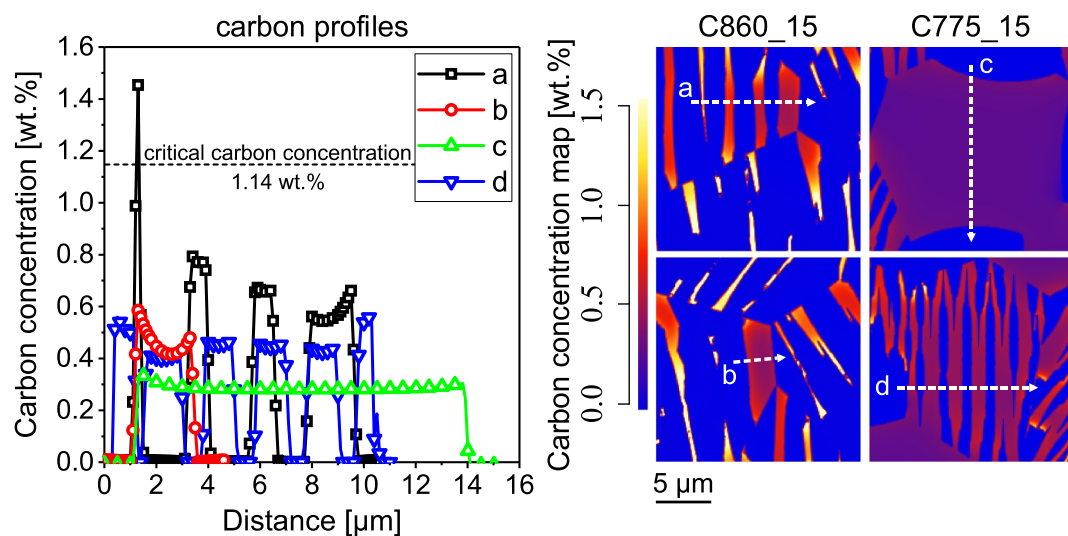


Fig. 14. Variations of carbon concentration along the indicated lines and across different areas in the microstructures of C860_15 (lines a and b) and C775_15 (lines c and d) simulated by means of phase field modeling.

5. Conclusions

In the present paper, the correlations of post-carburizing heat treatment-core microstructure-mechanical properties in a case hardening steel were investigated. The results derived from this study are summarized as follows:

1. At the hardening temperature of 775 °C, ferrite progressively develops in the core over time and enriches the remaining austenite with carbon. This retards and restricts the bainite transformation during the following quenching stage and promotes the formation of martensite instead. The fraction of ferrite and martensite are therefore directly correlated to each other.
2. During the formation of bainitic ferrite, excess carbon atoms are partitioned into the neighboring austenite increasing its chemical stability. Thus, there is a direct relation between the fractions of bainite and retained austenite. Besides, the overall level of carbon enrichment and, hence, the overall fraction of retained austenite is determined by total fraction of bainitic ferrite and ferrite together.
3. The improvement of impact toughness properties is in direct proportion to the fraction of bainite and retained austenite and in inverse proportion to the fraction of ferrite and martensite. The effective role of bainite is attributed to the intrinsic structure with many intermediate grain boundaries deflecting the propagating cracks, therefore, enhancing the microstructure's resistance against crack propagation. The presence of film-like retained austenite is beneficial by blunting the crack tip during its propagation (TRIP effect). On the contrary, the boundaries of ferrite and martensite grains with a severe hardness difference can trigger crack nucleation giving rise to degraded toughness properties.
4. Despite substantial differences in volume fraction of microstructural phases, the overall hardness values are similar in all the investigated microstructures. In the specimens quenched from 860 °C, the overall hardness is largely dominated by bainite. In the ferrite-containing specimens, while fraction of ferrite increases, the fraction of martensite increases too, retaining the overall hardness similar to that in C860_15.
5. The results of the phase field modeling such as the predicted fractions of microstructural constituents, particularly the fraction and morphology of retained austenite and the corresponding level of carbon enrichment agree well with the experimental observations.

Acknowledgment

The financial support of this research provided by the German Federal Ministry of Education and Research (BMBF) through Grant No. 01DQ14003A is gratefully acknowledged. M. J. Deepu and G. Phanikumar kindly acknowledge the financial support from the Indo-German Science and Technology Centre (IGSTC), New Delhi, India, for the project “DP-Forge”.

Data availability

The raw/processed data required to reproduce these findings cannot be shared at this time as the data also forms part of an ongoing study.

References

- [1] G. Parrish, Carburizing: Microstructures and Properties, ASM International, Materials Park, OH, 1999.
- [2] G. Krauss, Microstructures and Properties of Carburized Steels, ASM Handbook Volume 4 1990 Heat Treating (ASM International), 1990, pp. 363–375.
- [3] Y. Wang, Z. Yang, F. Zhang, D. Wu, Microstructures and mechanical properties of surface and center of carburizing 23Cr2Ni2Si1Mo steel subjected to low-temperature austempering, Mater. Sci. Eng.: A 670 (2016) 166–177.
- [4] J. Grosch, Microstructure and properties of gas carburized steels, Comprehensive Materials Processing, Elsevier, 2014, pp. 379–411.
- [5] A. Bensely, S. Stephen Jayakumar, D. Mohan Lal, G. Nagarajan, A. Rajadurai, Failure investigation of crown wheel and pinion, Eng. Fail. Anal. 13 (2006) 1285–1292.
- [6] K. Fukuoka, K. Tomita, T. Shiraga, Examination of surface hardening process for dual phase steel and improvement of gear properties, JFE Tech. Rep. 15 (2010) 17–23.
- [7] B. Jiang, Z. Mei, L.-y. Zhou, G.-l. Liu, Z.-l. Wang, B. Huang, Y.-z. Liu, High toughness and multiphase microstructure transition product of carburizing steel by a novel heat treatment cooling process, Mater. Sci. Eng.: A 675 (2016) 361–370.
- [8] Z. Sami, S. Tahar, H. Mohamed, Microstructure and Charpy impact properties of ferrite–martensite dual phase API X70 linepipe steel, Mater. Sci. Eng.: A 598 (2014) 338–342.
- [9] J. Jiang, H. Wu, J. Liang, Di Tang, Microstructural characterization and impact toughness of a jackup rig rack steel treated by intercritical heat treatment, Mater. Sci. Eng.: A 587 (2013) 359–364.
- [10] E. Boyle, D.O. Northwood, R. Bowers, X. Sun, P. Bauerle, The effects of initial microstructure and heat treatment on the core mechanical properties of carburized automotive steels, Mater. Forum (2008) 44–54.
- [11] W. Li, T. Sakai, M. Wakita, S. Mimura, Influence of microstructure and surface defect on very high cycle fatigue properties of clean spring steel, Int. J. Fatigue 60 (2014) 48–56.
- [12] H. Farivar, U. Prahl, M. Hans, W. Bleck, Microstructural adjustment of carburized steel components towards reducing the quenching-induced distortion, J. Mater. Process. Technol. 264 (2019) 313–327.
- [13] G. Totten, M. Howes, T. Inoue, Handbook of Residual Stress and Deformation of Steel, ASM International, Materials Park, Ohio, 2002 (44073-0002).

- [14] E. Boyle, R. Bowers, D.O. Northwood, The use of navy C-ring specimens to investigate the effects of initial microstructure and heat treatment on the residual stress, retained austenite, and distortion of carburized automotive steels, in: E. Boyle, R. Bowers, D.O. Northwood (Eds.), Proceedings of the SAE World Congress & Exhibition, SAE International 400 Commonwealth Drive, Warrendale, PA, United States, 2007.
- [15] J. Li, Y. Feng, L. Tang, X. Wu, FEM prediction of retained austenite evolution in cold work die steel during deep cryogenic treatment, *Mater. Lett.* 100 (2013) 274–277.
- [16] T. Sonar, S. Lomte, C. Gogte, V. Balasubramanian, Minimization of distortion in heat treated AISI D2 tool steel: mechanism and distortion analysis, *Procedia Manuf.* 20 (2018) 113–118.
- [17] W.C. Oliver, G.M. Pharr, An improved technique for determining hardness and elastic modulus using load and displacement sensing indentation experiments, *J. Mater. Res.* 7 (1992) 1564–1583.
- [18] MICRESS Group, The MICRostructure Evolution Simulation Software, <www.micress.de>.
- [19] K. Mukherjee, U. Prahl, W. Bleck, U. Reisgen, M. Schleser, A. Abdurakhmanov, Characterization and modelling techniques for gas metal arc welding of DP 600 sheet steels. Charakterisierung und Modellierungstechniken für Metallschutzgassschweißen von DP 600 Blech-Stählen, *Mat. -Wiss. U. Werkst.* 41 (2010) 972–983.
- [20] M. Tolouei, M. Militzer, Phase field modeling of the simultaneous formation of bainite and ferrite in TRIP steel, *Acta Mater.* 144 (2018) 786–800.
- [21] M.G. Mecozzi, J. Eiken, M.J. Santofimia, J. Sietsma, Phase field modelling of microstructural evolution during the quenching and partitioning treatment in low-alloy steels, *Comput. Mater. Sci.* 112 (2016) 245–256.
- [22] D.P. Koistinen, R.E. Marburger, A general equation prescribing the extent of the austenite-martensite transformation in pure iron-carbon alloys and plain carbon steels, *Acta Metall.* 7 (1959) 59–60.
- [23] K.W. Andrews, Empirical formulae for the calculation of some transformation temperatures, *J. Iron Steel Inst.* 203 (1965) 721–727.
- [24] G.F. Vander Voort, Metallography: Principles and Practice, McGraw-Hill, New York, N.Y., 1984.
- [25] B.C. Muddle, J.F. Nie, Formation of bainite as a diffusional-displacive phase transformation, *Scr. Mater.* 47 (2002) 187–192.
- [26] S.A. Mujahid, H.K.D.H. Bhadeshia, Coupled diffusional/displacive transformations: effect of carbon concentration, *Acta Metall. Mater.* 41 (1993) 967–973.
- [27] H.K.D.H. Bhadeshia, Bainite in Steels: Transformations, Microstructure and Properties, 2nd ed., IOM Communications, London, 2001.
- [28] J.G. Speer, D.V. Edmonds, F.C. Rizzo, D.K. Matlock, Partitioning of carbon from supersaturated plates of ferrite, with application to steel processing and fundamentals of the bainite transformation, *Curr. Opin. Solid State Mater. Sci.* 8 (2004) 219–237.
- [29] S. Li, G. Zhu, Y. Kang, Effect of substructure on mechanical properties and fracture behavior of lath martensite in 0.1C–1.1Si–1.7Mn steel, *J. Alloy. Compd.* 675 (2016) 104–115.
- [30] B. Wang, J. Lian, Effect of microstructure on low-temperature toughness of a low carbon Nb-V-Ti microalloyed pipeline steel, *Mater. Sci. Eng.: A* 592 (2014) 50–56.
- [31] Q. Zhou, L. Qian, J. Tan, J. Meng, F. Zhang, Inconsistent effects of mechanical stability of retained austenite on ductility and toughness of transformation-induced plasticity steels, *Mater. Sci. Eng.: A* 578 (2013) 370–376.
- [32] Z.J. Xie, S.F. Yuan, W.H. Zhou, J.R. Yang, H. Guo, C.J. Shang, Stabilization of retained austenite by the two-step intercritical heat treatment and its effect on the toughness of a low alloyed steel, *Mater. Des.* 59 (2014) 193–198.
- [33] G. Gao, H. Zhang, X. Gui, P. Luo, Z. Tan, B. Bai, Enhanced ductility and toughness in an ultrahigh-strength Mn–Si–Cr–C steel: the great potential of ultrafine filmy retained austenite, *Acta Mater.* 76 (2014) 425–433.
- [34] J. Zhang, H. Di, Y. Deng, R.D.K. Misra, Effect of martensite morphology and volume fraction on strain hardening and fracture behavior of martensite–ferrite dual phase steel, *Mater. Sci. Eng.: A* 627 (2015) 230–240.
- [35] G. Krauss, Martensite in steel, *Mater. Sci. Eng.: A* 273–275 (1999) 40–57.
- [36] M.J. Santofimia, L. Zhao, J. Sietsma, Microstructural evolution of a low-carbon steel during application of quenching and partitioning heat treatments after partial austenitization, *Metall. Mater. Trans. A* 40 (2009) 46–57.
- [37] H. Farivar, S. Richter, M. Hans, A. Schwedt, U. Prahl, W. Bleck, Experimental quantification of carbon gradients in martensite and its multi-scale effects in a DP steel, *Mater. Sci. Eng.: A* 718 (2018) 250–259.
- [38] M.J. Santofimia, C. Kwakernaak, W.G. Sloof, L. Zhao, J. Sietsma, Experimental study of the distribution of alloying elements after the formation of epitaxial ferrite upon cooling in a low-carbon steel, *Mater. Charact.* 61 (2010) 937–942.
- [39] S.S. Ghasemi Banadkouki, E. Fereiduni, Effect of prior austenite carbon partitioning on martensite hardening variation in a low alloy ferrite–martensite dual phase steel, *Mater. Sci. Eng.: A* 619 (2014) 129–136.
- [40] E. Fereiduni, S.S. Ghasemi Banadkouki, Reliability/unreliability of mixture rule in a low alloy ferrite–martensite dual phase steel, *J. Alloy. Compd.* 577 (2013) 351–359.